Chemical Engineering Journal 531 (2026) 173932

Contents lists available at ScienceDirect

Chemical Engineering Journal

journal homepage: www.elsevier.com/locate/cej

The application of nitrogen isotopic labelling in *operando* powder neutron diffraction studies of metal nitride ammonia synthesis catalysts☆

Li Shao [a], Angela Daisley [b], Marianna Casavola [a], Andrew L. Hector [a], Justin S.J. Hargreaves [b,*]

[a] School of Chemistry and Chemical Engineering, University of Southampton, Highfield, Southampton, SO17 1BJ, UK
[b] School of Chemistry, University of Glasgow, Glasgow, G12 8QQ, UK

ARTICLE INFO

Keywords:
Nitride
Ammonia
Neutron
Diffraction

ABSTRACT

Recently we found that doping tungsten into Co_3Mo_3N reduces its ammonia synthesis activity, despite indications that nitrogen is still mobile in its lattice and similar energies for surface nitrogen vacancy formation. In this short paper, we demonstrate *operando* powder neutron diffraction (PND) to directly compare the behaviour of Co_3Mo_3N and W-doped $Co_3Mo_{2.6}W_{0.4}N$ as a method to understand nitrogen exchange and mobility differences. PND is ideal for this purpose due to the large scattering length of nitrogen (9.37 fm natural abundance or ^{14}N 9.36 fm) and good contrast with ^{15}N (6.44 fm), that lead to sensitivity to nitrogen site behaviours during the changes.

1. Introduction

Due to its pivotal role in supporting 40% of the global population by provision of an accessible route to synthetic fertiliser, the study of ammonia synthesis is of enduring interest [1]. Industrial scale ammonia synthesis is accomplished via the Haber Bosch Process, which when considered in its entirety including the feedstock generation, is responsible for ca. 2% of global energy demand and ca. 1.6% of anthropogenic CO_2 emissions [2]. In recent years, attention has been directed towards development of sustainable ammonia synthesis where, for example, synthesis of fertiliser on local and small scale could be accomplished using hydrogen derived from water splitting with electricity derived from wind or solar power [3]. This would require the development of catalysts which were able to be applied under more moderate reaction conditions (lower pressure, lower temperature) than highly centralised Haber Bosch production as well as withstanding transient operation reflecting, for example, the intermittent nature of wind derived electricity.

One area of ammonia synthesis catalyst development has focused upon the possible application of metal nitrides as catalysts, one aspect of which may be the potential to operate via the Mars-van Krevelen pathway wherein transient production and replenishment of lattice nitrogen vacancies is pivotal [3]. Whilst this potential mechanism is not universally accepted as being operational or significant for all nitride systems [4], there has been experimental evidence for operation in some systems which has found support through computational modelling [5–9]. As has also been the case for other classes of ammonia synthesis catalyst, fundamental mechanistic insight has been achieved by application of isotopic nitrogen exchange [10]. For example homomolecular exchange (which involves the isotopic scrambling of $^{14}N_2$ and $^{15}N_2$ from a gas-phase mixture) provides information on the ability of a material to activate, dissociate, recombine and desorb N_2 and heterolytic exchange which involves the reaction of $^{15}N_2$ with a nitride material (which predominantly comprises ^{14}N reflecting natural isotopic abundance) provides an indication of nitrogen activation, active and mobile lattice nitrogen reactivity, and nitrogen desorption. Isotopic exchange measurements are generally conducted in the absence of the co-reactant hydrogen under conditions generally far removed from those corresponding to the operational state of the catalysts involved. Therefore, it would be of interest to demonstrate additional approaches towards assessing the reactivity of lattice nitrogen under reaction conditions.

In this short paper, we demonstrate the application of *operando* powder neutron diffraction (PND). When using an isotopically labelled reaction feed it is possible to track lattice nitrogen under reaction conditions since ^{14}N and ^{15}N possess significantly different neutron scattering coefficients. The system which we have selected for investigation is Co_3Mo_3N, which has been established as an effective ammonia synthesis catalyst and chemical looping reagent [11–14] and for which

☆ This article is part of a Special issue entitled: 'Harold Kung – A Career in ChE' published in Chemical Engineering Journal.

* Corresponding author.
E-mail address: Justin.Hargreaves@glasgow.ac.uk (J.S.J. Hargreaves).

https://doi.org/10.1016/j.cej.2026.173932
Received 28 November 2025; Received in revised form 29 January 2026; Accepted 7 February 2026
Available online 9 February 2026

reversible lattice nitrogen loss has been documented and the lattice nitrogen vacancy formation, dinitrogen activation and ammonia synthesis mechanism has been computationally modelled [8,9]. Furthermore, the Co_2Mo_3N impurity phase is also present for which it is known that the lattice nitrogen is much more stable [15,16]. We also report the performance of a corresponding tungsten doped system.

2. Experimental

2.1. Chemicals

Cobalt nitrate hexahydrate ($Co(NO_3)_2{\cdot}6H_2O$, 99%), ammonium metatungstate tetrahydrate ($(NH_4)_6H_2W_{12}O_{40}{\cdot}4H_2O$, 99.99%), and ammonium heptamolybdate tetrahydrate ($(NH_4)_6Mo_7O_{24}{\cdot}4H_2O$, ≥99.0%) were obtained from Sigma-Aldrich. Nitric acid (70%) and citric acid monohydrate (99.5%) were purchased from Thermo Fisher Scientific. Ammonia (99.94%) and nitrogen (industrial grade, oxygen-free) gases were supplied by BOC Ltd.

2.2. Catalyst synthesis

The samples were prepared via a citrate gel route followed by ammonolysis [17].

For the synthesis of Co_3Mo_3N, 11.27 mmol of $Co(NO_3)_2{\cdot}6H_2O$ and 1.61 mmol of $(NH_4)_6Mo_7O_{24}{\cdot}4H_2O$ were dissolved in 60 mL of a 2.6 mol L^{-1} aqueous nitric acid (HNO_3) solution. 37.8 mmol of citric acid monohydrate was subsequently added to the resulting pink precursor aqueous solution. The solution was evaporated in a sand bath at 70 °C until a viscous pink gel (~10 cm^3) was obtained and no free liquid remained. The gel was transferred to a crucible and heated in an ashing furnace in air at 500 °C for 2 h using a heating rate of 60 °C min^{-1}. The resulting foam was ground into a powder and transferred to a boat crucible, which was placed inside a quartz tube furnace equipped with gas inlet and outlet valves. The sample was heated under flowing anhydrous ammonia (BOC, 99.94%, further dried over molecular sieves) at a heating rate of 5 °C min^{-1} to 900 °C and maintained at this temperature for 12 h. The ammonia flow rate was 40 mL/min. After natural cooling to room temperature, the furnace tube was flushed with nitrogen for 30 min using a Schlenk line (nitrogen flow corresponding to 2 bubbles per second). Subsequently, air was introduced gradually to allow controlled passivation of the sample surfaces. The black crystalline product was then collected.

The W-doped sample $Co_3Mo_{2.6}W_{0.4}N$ was synthesised using a similar procedure. In this case, 11.27 mmol of $Co(NO_3)_2{\cdot}6H_2O$, 0.125 mmol of $(NH_4)_6H_2W_{12}O_{40}{\cdot}4H_2O$, and 1.395 mmol of $(NH_4)_6Mo_7O_{24}{\cdot}4H_2O$ were dissolved in 60 mL of 2.6 mol L^{-1} HNO_3 solution, followed by the addition of 37.8 mmol of citric acid monohydrate to form the precursor solution.

The chemical compositions of these two samples were investigated by EDX in our previous work [17]. As shown in Table S1, the atomic ratios of Mo are higher than the theoretical values for $Co_3Mo_{2.6}W_{0.4}N$ and Co_3Mo_3N and the ratios of Co are similar to the theoretical values.

2.3. Structural characterisation

X-ray diffraction (XRD) patterns of Co_3Mo_3N and $Co_3Mo_{2.6}W_{0.4}N$ were collected with a Rigaku Smartlab employing Cu-K_α X-rays and a HyPix detector in 1D mode over the 2θ range of 10–80°. Co_3Mo_3N and $Co_3Mo_{2.6}W_{0.4}N$ were measured by *operando* PND using the Polaris diffractometer at the ISIS Neutron and Muon Source. The *in situ* cell used in the *operando* experiment is made from stainless steel with internal diameter of 11 mm and wall thickness of 0.3 mm. A flow-through setup was used, where gas entered at the bottom and flowed up through the sample. A constant gas flow rate of 60 mL/min was used for all gas compositions. The temperature was increased at a constant heating ramp rate of 10 °C min^{-1} during the PND measurements. Each of the ~1 g samples were loaded in the cell and first heated in a mixture of 75% H_2 and 25% N_2 from room temperature to 650 °C at 10 °C min^{-1}. A series of changes of gas environments were then applied at 650 °C to change the composition of the nitrogen atom sites. The processes were conducted at this temperature to enable bulk phase transitions in the materials under the different gas atmospheres. At lower temperatures, the transformation of Co_3Mo_3N to Co_6Mo_6N under 3:1 H_2/Ar is not observed [7]. The *operando* PND procedure is shown below:

Step 1. Flowing 75% H_2 and 25% N_2 at room temperature.
Step 2. Heating to 650 °C at 10 °C min^{-1} under 75% H_2 and 25% N_2 to ensure full nitridation of the sample.
Step 3. Switching to 75% H_2 and 25% Ar to remove nitrogen from the lattice, assessing nitrogen mobility. Previous studies have shown that in Co_3Mo_3N, approximately half of the nitrogen can be removed, with a relocation of the residual N from the 16c to the 8a site [7]. Co_3Mo_3N has a structure consisting of a distorted face centred cubic (fcc) arrangement of the Co atoms. The nitrogen atom is located in the interstitial site and is surrounded by six Mo atoms to form an Mo_6N octahedron [18]. These octahedra are corner sharing. In Co_6Mo_6N, the nitrogen is located in the 8a octahedral Wyckoff site, resulting in a contraction of the sublattice due to the distances in the Co sublattice decreasing [7]. The Mo − N distance increases by approximately 1% and the Mo_6N octahedra are no longer distorted.
Step 4. Reintroducing 3:1 ratio of H_2 and N_2 to repopulate the vacancies, with the expectation that 16c sites will be reoccupied. This tests the ability to accept nitrogen from the gas phase.
Step 5. Flowing 75% H_2 and isotopic 25% $^{15}N_2$ to test the rate of exchange under typical catalytic conditions.

For each experimental step, PND data were collected continuously in 10-min scans. These short scans were used to monitor the dynamic evolution of crystalline phases during changes in the gas atmosphere. A longer (1 h) acquisition was made when no further significant phase evolution was observed, to obtain data suitable for high-quality Rietveld refinement. The longer scan was acquired directly, rather than by summing multiple short scans, to minimise uncertainties associated with transient structural changes.

2.4. PND data fitting and analysis

A boron nitride ceramic and gadolinium foil collimator fitted around the *in situ* cell, allowed the diffraction pattern collected in the Polaris 2theta = 90° detectors to be free from Bragg reflections off the stainless steel. Bank 4 was used to collect the diffraction data. The obtained PND data were analysed using the GSAS-II software package [19]. A Chebyshev-1 background function with 8–10 coefficients was employed for data of Co_3Mo_3N and 10–13 coefficients for data of $Co_3Mo_{2.6}W_{0.4}N$. Peak profiles were modelled using the GSAS-II default pseudo-Voigt function, which combines Gaussian and Lorentzian contributions. The refinement range was set from 3000 to 19,927 μs TOF. The peak shape is defined by an Ikeda-Carpenter-pseudo-Voigt function, with the initial parameters defined by refinement of the pattern from a vanadium rod.

In this work, all PND data were converted from a TOF-based x-axis to the scattering vector q using the GSAS-II package. In a typical refinement, the background coefficients, sample absorption, lattice parameters, and phase fractions and nitrogen site occupancies of all identified phases were refined. Crystallite size and microstrain parameters were not refined and were kept at GSAS-II default values. For W-doped sample, W atoms were constrained to share the Mo atomic sites, with the Mo:W ratio fixed at 0.8667:0.1333 during refinement. For the two samples under room temperature and 3:1 H_2/N_2, three phases were observed, including the main phase cubic *Fd*-3*mz* Co_3Mo_3N structure (ICSD 37505) ($Co_3Mo_{2.6}W_{0.4}N$ for W-doped sample), and two impurity phases: $P4_132$ Co_2Mo_3N (ICSD 96417) ($Co_2Mo_{2.6}W_{0.4}N$ for W-doped sample) and *F*-43*m* $CoCo_2O_4$ (ICSD 9362).

The weight fraction of the cobalt oxide impurity phase was low, and several cobalt oxide phases with similar but slightly shifted peak positions may be present (e.g., CoO, Co_3O_4, $CoO_{1.92}$). For consistency across the PND refinements and to avoid over parameterisation, $CoCo_2O_4$ (ICSD 9362) was used as a representative cobalt oxide phase in the structural modelling, as it reasonably reproduces the characteristic peak positions. However, due to the possible coexistence of multiple cobalt oxides, this phase could not be fitted with high precision. Consequently, the isotropic displacement parameter (U_{iso}) of Co in $CoCo_2O_4$ was constrained to relatively large fixed values (0.1–0.41 $Å^2$) to account for modelling uncertainty rather than being refined freely. All atom tables from the Rietveld fits are reported in the Supporting Information.

3. Results and discussion

All the PND data of $Co_3Mo_{2.6}W_{0.4}N$ and Co_3Mo_3N at each stage are listed in Fig. S1 and Fig. S2. Room-temperature PND Rietveld refinements collected under a 3:1 H_2/N_2 atmosphere for $Co_3Mo_{2.6}W_{0.4}N$ and Co_3Mo_3N are presented in Fig. 1 and S3, respectively, with the corresponding atomic tables provided in Tables S2 and S3. Refined parameters for both materials are summarised in Tables 1 and 2. The term ^{14}N fraction in the tables refers to the weight fraction of nitrogen atoms present as the ^{14}N isotope in the phase, used to distinguish these from the ^{15}N atoms introduced in Stage 5. In Stages 1–4, only natural nitrogen ("N", i.e.^{14}N) was considered and refined. Accordingly, ^{14}N is shown in Tables 1 and 2 instead of "N" to avoid isotopic ambiguity.

The PND patterns are plotted in q-space. In each case, the dominant phase is cubic *Fd-3mz* Co_3Mo_3N structure (ICSD 37505), with refined weight fractions of 82.5% for Co_3Mo_3N and 79.3% for $Co_3Mo_{2.6}W_{0.4}N$. Two impurity phases were identified: $P4_132$ Co_2Mo_3N (ICSD 96417) for both samples ($Co_2Mo_{2.6}W_{0.4}N$ for the W-doped sample) and *F*-43 *m* $CoCo_2O_4$ (ICSD 9362). This is in agreement with previous publications showing that Co_2Mo_3N can form as an impurity during Co_3Mo_3N synthesis [20,21]. As expected, the refined nitrogen occupancies are high in both materials, exceeding 90%.

The refinements show that for the W-doped sample $Co_3Mo_{2.6}W_{0.4}N$, tungsten was incorporated into both the main Co_3Mo_3N phase and Co_2Mo_3N impurity phase. These phases are therefore referred to as $Co_3Mo_{2.6}W_{0.4}N$ and $Co_2Mo_{2.6}W_{0.4}N$, respectively. W atoms were constrained to share the Mo atomic sites, with the Mo:W ratio fixed at 0.8667:0.1333 during refinement. Tungsten was not introduced into the $CoCo_2O_4$ phase because its low phase fraction and limited data quality.

In Fig. 1, the main peaks below q = 6 $Å^{-1}$ are labelled. The most intense peaks are from the main $Co_3Mo_{2.6}W_{0.4}N$ phase and are marked with "*". The only exception is the intense peak at q = 3.1 $Å^{-1}$, which corresponds to the 2 2 2 reflection of $CoCo_2O_4$ and is labelled with "Δ". Several small features adjacent to intense reflections arise from the $Co_2Mo_{2.6}W_{0.4}N$ impurity and are marked with "#". These include peaks at q = 2.83 $Å^{-1}$, 3.00 $Å^{-1}$, 3.13 $Å^{-1}$, and 3.27 $Å^{-1}$, assigned to the 2 2 1, 3 1 0, 3 1 1, and 2 2 2 reflections, respectively. Similarly, Fig. S3 shows the three phases of Co_3Mo_3N with slightly lower impurity fractions.

The PND results are consistent with the XRD patterns (Fig. 2), which also show that Co_3Mo_3N and $Co_3Mo_{2.6}W_{0.4}N$ as the dominant phases. The main impurity observed in XRD is Co_2Mo_3N (ICSD 96417), with its reflections marked by "#". $CoCo_2O_4$ reflections are not clearly observed in the XRD patterns but are evident in the PND data. The peak at q ≈ 3.05 $Å^{-1}$ in the XRD pattern is likely due to a cobalt oxide impurity, however, its position does not match that of $CoCo_2O_4$ exactly. As discussed in the "PND data fitting and analysis" section, several cobalt oxide phases may be present in small quantities. For consistency across datasets, $CoCo_2O_4$ was used as a representative cobalt oxide phase in the refinements, even though its XRD signal is weak.

$Co_3Mo_{2.6}W_{0.4}N$ exhibits similar reflections in both the PND and XRD patterns. The 2 2 4, 1 5 1, 3 3 3, and 4 4 0 reflections are intense under both X-ray and neutron beams. The PND data additionally reveal several weaker reflections, including 2 2 2, 5 3 1, 6 6 0, and 8 4 0. This highlights

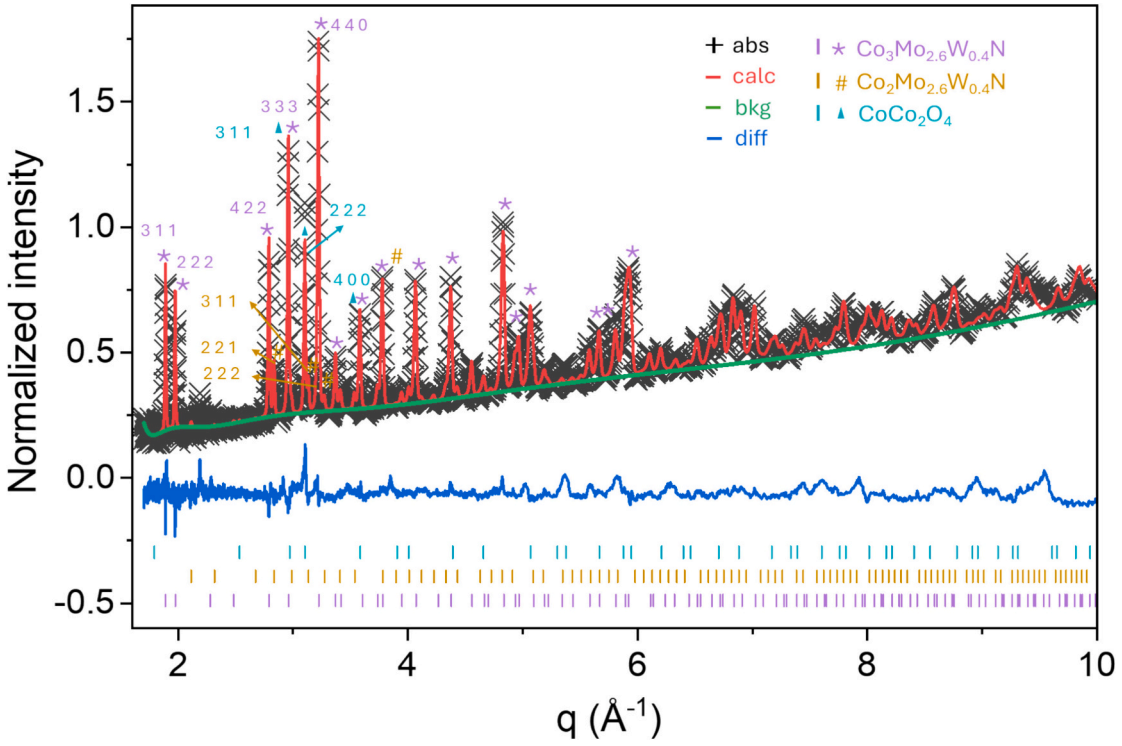

Fig. 1. (Step 1) Rietveld refinement of the PND pattern of $Co_3Mo_{2.6}W_{0.4}N$ collected at room temperature under a 3:1H_2/N_2 atmosphere. The black crosses represent the experimental data, the red line corresponds to the calculated pattern, the green line indicates the background, and the blue line shows the difference between the experimental and calculated patterns. Purple tick marks denote the allowed reflections of the Fd-3mz Co_3Mo_3N-type phase, while the brown and cyan tick marks indicate reflections from the $P4_132$ Co_2Mo_3N-type phase and F-43 m $CoCo_2O_4$. respectively.

Table 1
Summary of phase information for Co_3Mo_3N at each experimental step, including the identified phases, unit-cell parameter a, phase weight fractions, and nitrogen content.

Step	Co_3Mo_3N			Co_2Mo_3N			$CoCo_2O_4$	
	Unit cell a	Wt. frac	^{14}N frac	Unit cell a	Wt. frac	^{14}N frac	Unit cell a	Wt. frac
1: 75% H_2 + 25% N_2; RT	11.0247(3)	0.825(8)	0.911(8)	6.6506(17)	0.123(8)	0.80(7)	7.0033(14)	0.0516(19)
2: 75% H_2 + 25% N_2; 650 °C	11.0962(3)	0.834(5)	0.906(7)	6.6853(11)	0.140(5)	0.74(3)	7.0767(12)	0.0257(8)
3: 75% H_2 + 25% Ar; 650 °C[a]	11.0985(3)	0.568(4)	0.909(8)	6.6862(11)	0.126(6)	0.89(4)	7.0773(12)	0.0449(13)
4: 75% H_2 + 25% N_2; 650 °C	11.0964(3)	0.8208(10)	0.998(10)	6.6853(11)	0.1376(2)	0.633(25)	7.0774(11)	0.0416(12)
5: 75% H_2 + 25% ^{15}N; 650 °C[b]	11.0963(3)	0.798(5)	0.009(1)	6.6845(12)	0.157(5)	0.006(9)	7.0768(12)	0.0452(14)

[a] Also contains Co_6Mo_6N, see text for parameters.
[b] Co_3Mo_3N contains ^{15}N at full occupancy.

Table 2
Summary of phase information for $Co_3Mo_{2.6}W_{0.4}N$ at each experimental step, including the identified phases, unit-cell parameter a, phase weight fractions, and nitrogen content.

Step	$Co_3Mo_{2.6}W_{0.4}N$			$Co_2Mo_{2.6}W_{0.4}N$			$CoCo_2O_4$	
	Unit cell a	Wt. frac	^{14}N frac	Unit cell a	Wt. frac	^{14}N frac	Unit cell a	Wt. frac
1: 75% H_2 + 25% N_2; RT	11.0241(5)	0.793(7)	0.946(18)	6.6470(17)	0.089(6)	0.98(8)	7.0107(6)	0.119(4)
2: 75% H_2 + 25% N_2; 650 °C	11.0958(4)	0.736(5)	0.930(10)	6.6837(14)	0.099(5)	0.77(6)	7.0812(5)	0.165(2)
3: 75% H_2 + 25% Ar; 650 °C[a]	11.1010(13)	0.263(5)	1.01(3)	6.6839(20)	0.101(7)	0.42(9)	7.0817(7)	0.147(3)
4: 75% H_2 + 25% N_2; 650 °C	11.0951(5)	0.737(6)	0.995(20)	6.6828(18)	0.110(5)	0.35(6)	7.0818(6)	0.157(3)
5: 75% H_2 + 25% ^{15}N; 650 °C[b]	11.0948(6)	0.74287(16)	0.007(10)	6.682(2)	0.103(2)	0.02(7)	7.0813(6)	0.154(3)

[a] Also contains W-doped Co_6Mo_6N, see text for parameters.
[b] $Co_3Mo_{2.6}W_{0.4}N$ contains ^{15}N at 0.991(9) occupancy.

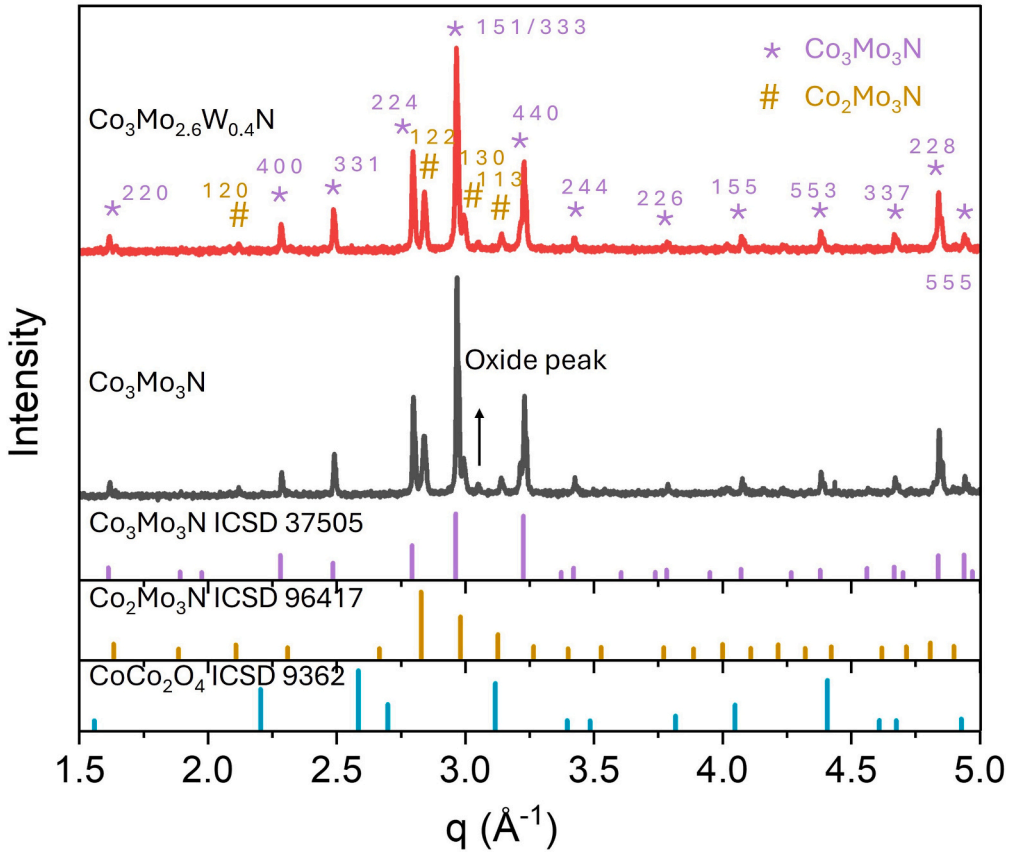

Fig. 2. XRD patterns of Co_3Mo_3N and $Co_3Mo_{2.6}W_{0.4}N$ prior to PND measurements. The reference pattern for Co_3Mo_3N (ICSD 37505), Co_2Mo_3N (ICSD 96417) and $CoCo_2O_4$ (ICSD 9362) are also shown for comparison. Peaks corresponding to the main Co_3Mo_3N phase are marked with "*", while peaks attributed to impurity phases are marked with "#". $CoCo_2O_4$ peaks are not observed in XRD but are evident in the PND patterns. The peak at $q \approx 3.05$ Å^{-1} is likely to originate from a cobalt oxide impurity.

the enhanced sensitivity of neutrons to light elements and enables more precise refinement of minor features. Overall, the higher resolution of

the PND patterns results in improved accuracy in identifying impurity reflections and refining phase fractions.

The 3:1H_2/N_2 atmosphere was maintained while the temperature was increased to 650 °C in Step 2. The refined PND patterns of $Co_3Mo_{2.6}W_{0.4}N$ and Co_3Mo_3N under these conditions are provided in Figs. 3 and S4, with atom tables in Tables S4 and S5. For both phases, the refined parameters include the unit cell parameters, the phase fraction, the nitrogen weight fraction and U_{iso}, and U_{iso} of "Co" in $CoCo_2O_4$. As expected, the lattice parameters of both main phases increased due to thermal expansion (Tables 1 and 2), by 0.65%. The impurity phases also exhibited lattice expansion with increasing temperature. The refined weight fractions of each phase are also given at each stage, with variations likely reflecting uncertainty in this parameter rather than real chemical changes. For the main phase of Co_3Mo_3N and $Co_3Mo_{2.6}W_{0.4}N$, the nitrogen content remains at high fractional occupancy levels, of 90.6% and 93.0% respectively, indicating the nitrogen is relatively stable at 650 °C under this gas environment.

The gas mixture was then changed to a 3:1 ratio of H_2/Ar to investigate the mobility of lattice nitrogen within these materials. Previous studies have shown that half the lattice nitrogen in Co_3Mo_3N can be removed to form Co_6Mo_6N under reducing conditions [7,22]. The remaining nitrogen is relocated from the 16c Wyckoff crystallographic site to the 8a site. Heterolytic isotopic exchange experiments also demonstrate that a large proportion of the Co_3Mo_3N lattice nitrogen can be exchanged [10]. Furthermore, computational modelling suggests that a substantial concentration of surface lattice vacancies are formed under ammonia synthesis conditions [8,9]. For Co_3Mo_3N, it is suggested that ammonia synthesis occurs via a Mars-van Krevelen mechanism, where the hydrogenation of lattice nitrogen results in the formation of ammonia and lattice nitrogen vacancies. In the case of W-doped Co_3Mo_3N, the nitrogen mobility within this catalyst has not been as well studied. In our previous work, it has been shown that the nitrogen is mobile in W-doped Co_3Mo_3N and these materials have similar surface nitrogen vacancy formation energies [17]. Therefore, it would be expected that some nitrogen would be removed from these materials under these conditions.

During the *operando* PND experiments, diffraction patterns were collected every 10 min while flowing 3:1 H_2/Ar at 650 °C. After approximately 200 min, a one-hour fine scan was collected to obtain a high signal-to-noise PND pattern. Figs. 4 and 5 show the Rietveld fits to the one-hour scans of Co_3Mo_3N and $Co_3Mo_{2.6}W_{0.4}N$, respectively, with the corresponding atom tables provided in Tables S6 and S7. For refinement, the Co_6Mo_6C structure (ICSD 198819, *Fd*-3 *m*) was included, with carbon replaced by nitrogen to represent Co_6Mo_6N. For all phases present, the refined parameters included the lattice parameters, phase fractions, and nitrogen site occupancies.

Compared with the patterns collected under N_2, an additional reflection at q = 2.3 $Å^{-1}$ appeared for both samples after flowing Ar. This reflection corresponds to the 4 0 0 peak of Co_6Mo_6N and is marked with "○" in Figs. 4 and 5. The emergence of this peak indicates the formation of the reduced Co_6Mo_6N phase. Upon reduction, the Co_3Mo_3N phase fraction decreased accordingly, while the other impurity phases remained at approximately the same levels (Tables 1 and 2). The Co_3Mo_3N phase retained lattice parameters and nitrogen occupancies similar to those observed under H_2/N_2. The reduction of Co_3Mo_3N resulted in 26.1(4) wt% Co_6Mo_6N with a = 10.9581(7) Å and the nitrogen sites 79(3)% occupied. The W-doped $Co_3Mo_{2.6}W_{0.4}N$ formed a larger fraction of the reduced $Co_6Mo_{5.2}W_{0.8}N$ phase (49.0(7) wt%) with a = 10.9567(8) Å and nitrogen sites 85%(3) occupied. These results show that the W-doped material more readily releases nitrogen under these conditions.

Rapid-scan PND patterns collected every 10 min were also analysed. By refining these quick scan datasets, the time evolution of the phase fractions could be monitored. The Co_6Mo_6N fraction in Co_3Mo_3N and the $Co_6Mo_{5.2}W_{0.8}N$ fraction in $Co_3Mo_{2.6}W_{0.4}N$ as a function of H_2/Ar exposure time are shown in Fig. 6. For the rapid scan refinements, only

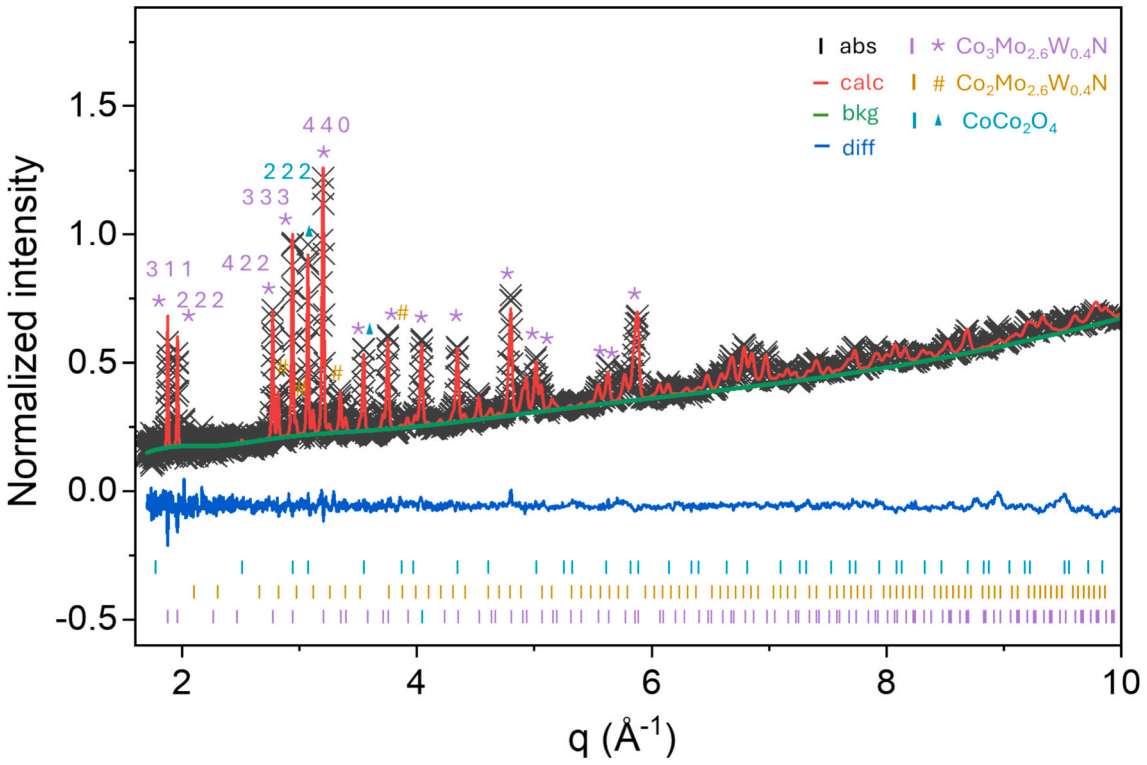

Fig. 3. (Step 2) Rietveld refinement of the PND pattern of $Co_3Mo_{2.6}W_{0.4}N$ collected at 650 °C under a 3:1H_2/N_2 atmosphere. The black crosses represent the experimental data, the red line corresponds to the calculated pattern, the green line indicates the background, and the blue line shows the difference between the experimental and calculated patterns. Purple tick marks denote the allowed reflections of the Fd-3mz Co_3Mo_3N-type phase, while the brown and cyan tick marks indicate reflections from the $P4_132$ Co_2Mo_3N-type phase and F-43 m $CoCo_2O_4$, respectively.

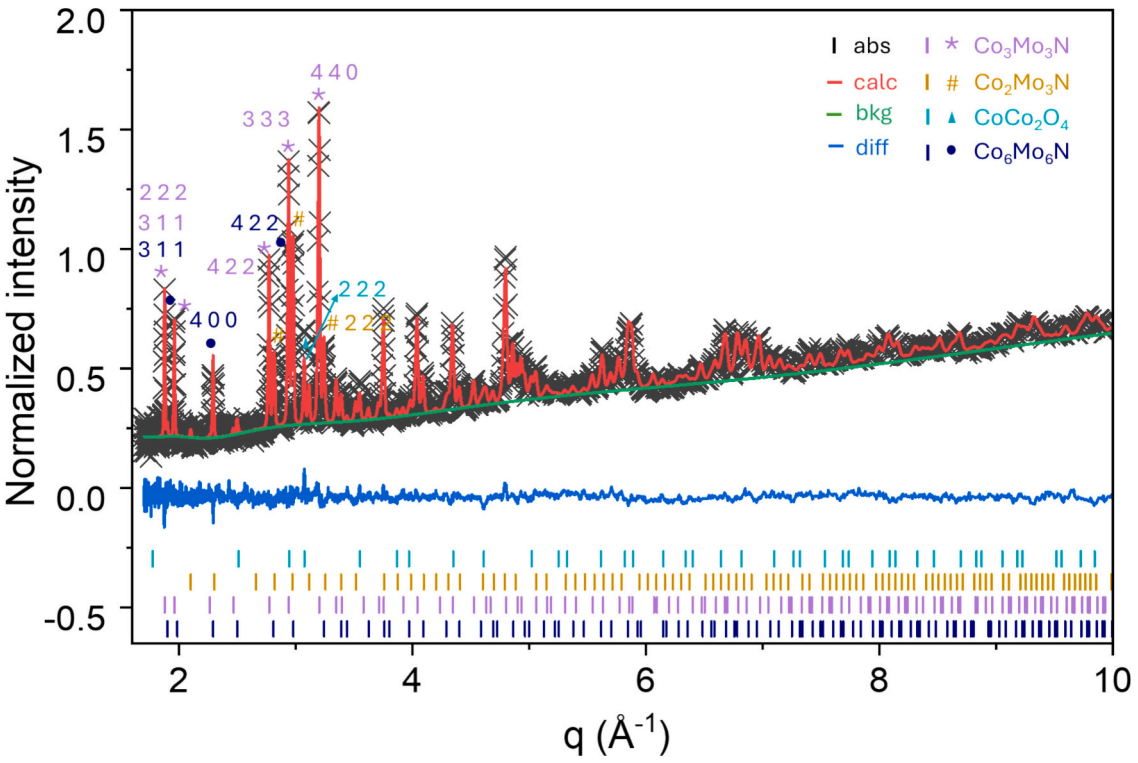

Fig. 4. (Step 3) Rietveld refinement of the PND pattern of Co_3Mo_3N collected at 650 °C under a 3:1H_2/Ar atmosphere. The black crosses represent the experimental data, the red line corresponds to the calculated pattern, the green line indicates the background, and the blue line shows the difference between the experimental and calculated patterns. Purple tick marks denote the allowed reflections of the Fd-3mz Co_3Mo_3N-type phase, while the brown and cyan tick marks indicate reflections from the $P4_132$ Co_2Mo_3N-type phase and F-43 m $CoCo_2O_4$, respectively. Dark blue tick marks denote the reflections from the Fd-3 m Co_6Mo_6N-type phase.

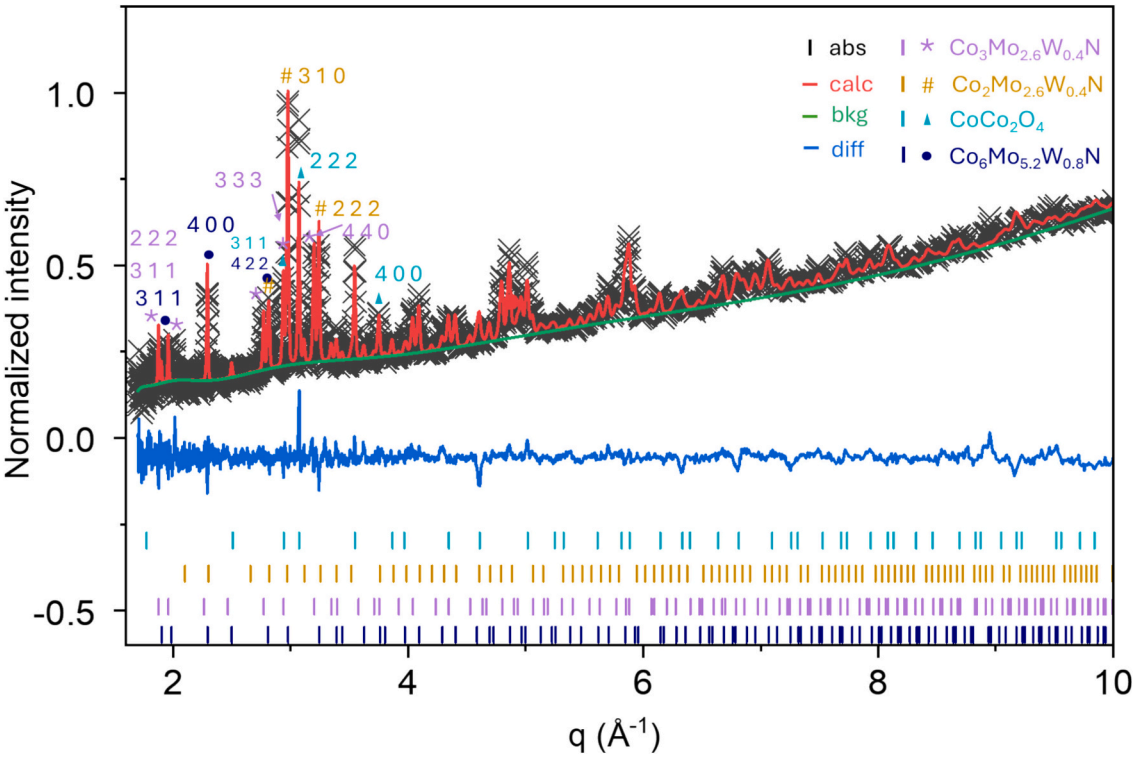

Fig. 5. (Step 3) Rietveld refinement of the PND pattern of $Co_3Mo_{2.6}W_{0.4}N$ collected at 650 °C under a 3:1H_2/Ar atmosphere. The black crosses represent the experimental data, the red line corresponds to the calculated pattern, the green line indicates the background, and the blue line shows the difference between the experimental and calculated patterns. Purple tick marks denote the allowed reflections of the Fd-3mz Co_3Mo_3N-type phase, while the brown and cyan tick marks indicate reflections from the $P4_132$ Co_2Mo_3N-type phase and F-43 m $CoCo_2O_4$, respectively. Dark blue tick marks denote the reflections from the Fd-3 m Co_6Mo_6N-type phase.

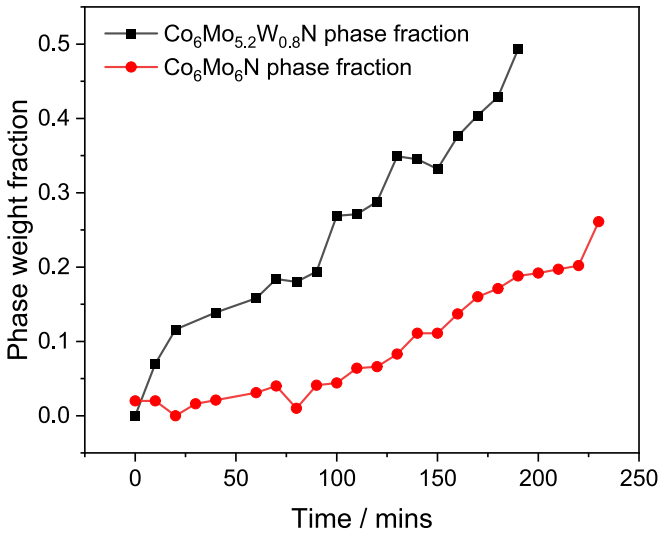

Fig. 6. (Step 3) Evolution of Co_6Mo_6N and $Co_6Mo_{5.2}W_{0.8}N$ phase fractions with time at 650 °C under a 3:1 H_2/Ar atmosphere. Full time-resolved phase fraction data are provided in Tables S8 and S9.

the phase fractions and nitrogen occupancies were refined, while all other parameters were fixed to the values obtained from the one-hour scans (Tables S6 and S7). Full time-resolved phase fraction data are provided in Tables S8 and S9. The characteristic 4 0 0 reflection of the Co_6Mo_6N-type phase appeared in the $Co_3Mo_{2.6}W_{0.4}N$ sample immediately after switching to Ar, and after 10 min the $Co_6Mo_{5.2}W_{0.8}N$ fraction exceeded 10%. In contrast, Co_3Mo_3N required more than 130 min under identical conditions before the Co_6Mo_6N phase became detectable (>10%).

The most obvious observation is that transformation of $Co_3Mo_{2.6}W_{0.4}N$ to form $Co_6Mo_{5.2}W_{0.8}N$ occurs more quickly than Co_3Mo_3N to Co_6Mo_6N. Neither process was complete after 200 or 240 min, respectively, so the larger conversion of the W-doped phase observed in the full Rietveld fits can be attributed to this kinetic effect. It appears that doping with W facilitates the removal of lattice nitrogen from these materials. The ammonia synthesis activity of $Co_3Mo_{2.6}W_{0.4}N$ is reported to be lower than for Co_3Mo_3N [17]. This suggests that while lattice nitrogen mobility may be an important factor in ammonia synthesis activity, other factors also play a significant role. For the Mars-van Krevelen mechanism, it is possible that only nitrogen at the surface and sub-surface regions participate in the reaction and nitrogen vacancies are regenerated from gas phase nitrogen or migration of sub-surface nitrogen species. For example, the bulk lattice nitrogen reactivity of Fe_3Mo_3N appears to be minimal under 3:1 H_2/Ar up to 800 °C [23]. However, computational modelling suggests that a surface-based Mars-van Krevelen mechanism can operate for Fe_3Mo_3N, although at a reduced rate compared to Co_3Mo_3N due to a lower concentration of surface nitrogen vacancies [24]. Therefore, important factors that have an impact on the activity are the vacancy formation energy and N_2 adsorption and activation at the vacancy site. However, as there is no difference in energies between the formation of surface nitrogen vacancies or the N_2 adsorption for Co_3Mo_3N and $Co_3Mo_{2.6}W_{0.4}N$, this cannot be a contributing factor for these materials [17]. Instead, doping with W may inhibit subsequent hydrogenation steps. Previous computational studies suggest that the rate determining process for Co_3Mo_3N is the hydrogenation of lattice nitrogen to regenerate the vacancies [9].

Co_3Mo_3N can be regenerated from Co_6Mo_6N upon exposure with 3:1 H_2:N_2 at 400 °C or by using N_2 at a higher temperature of 700 °C [3]. To investigate the ability of these materials to accept nitrogen from the gas phase, the atmosphere was changed back to a 3:1 ratio of H_2/N_2 in Step 4. Fig. 7 shows the phase fractions versus time under flowing nitrogen. At the end of Step 4, 1-h fine scans were conducted for the two

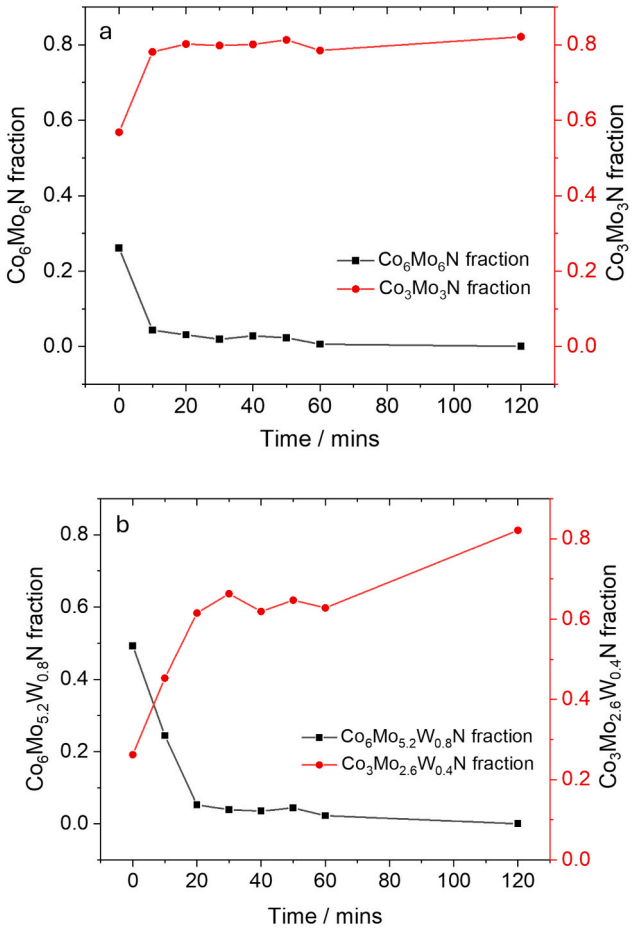

Fig. 7. (Step 4) Phase fractions versus time for the materials at 650 °C under 3:1 H_2/N_2. (a) Co_3Mo_3N and Co_6Mo_6N and (b) $Co_3Mo_{2.4}W_{0.6}N$ and $Co_6Mo_{5.2}W_{0.8}N$.

samples and the PND patterns are displayed in Figs. S5 and S6, with atom tables in Tables S10 and S11. For both phases, the refined parameters include the unit cell parameters, the phase fraction, and the nitrogen weight fraction. There is some scatter in the plots reflecting some uncertainty in the refined phase fractions. However, Fig. 7(a) shows the Co_6Mo_6N weight fraction decreased sharply from 26.1% to 4.3% within the first 10 min, followed by a gradual reduction to zero. Sample $Co_3Mo_{2.6}W_{0.4}N$ shows a slower nitrogen repopulation rate, as shown in Fig. 7(b). During the first 10 min of exposure to 3:1 H_2:N_2, the weight fraction of the reduced phase $Co_6Mo_{5.2}W_{0.8}N$ decreased from 49.0% to 24.4%. After 20 min under nitrogen, 5.2 wt% of this reduced phase remained. Overall, both materials showed rapid nitrogen vacancy repopulation after introducing of the 3:1 H_2:N_2 atmosphere, resulting in the transformation of the reduced phases back to their original nitride structures. After Step 4, the phase fractions of Co_3Mo_3N and $Co_3Mo_{2.6}W_{0.4}N$ were similar to those previously reported values of 82.1% and 73.7% in Step 2.

Isotopic exchange studies have previously shown that heterolytic $^{15}N_2$ exchange can occur in Co_3Mo_3N in the absence of hydrogen at 600 °C, with 25% of the total number of nitrogen replaced after 40 min [10]. Therefore, it would be of interest to further investigate the mobility of lattice nitrogen within these systems by introducing gas phase isotopic $^{15}N_2$. ^{15}N has a different scattering ability (6.44 fm) compared to ^{14}N (9.36 fm), which allows the opportunity to probe the bulk nitrogen site exchange during reaction. The ^{15}N weight fractions in Co_3Mo_3N and $Co_3Mo_{2.6}W_{0.4}N$ under 3:1 $H_2/^{15}N_2$ versus time are presented in Fig. 8. The values are from the refinement of 10 min short scans. Figs. S7 and S8 show the Rietveld fits to the 1-h scan PND patterns

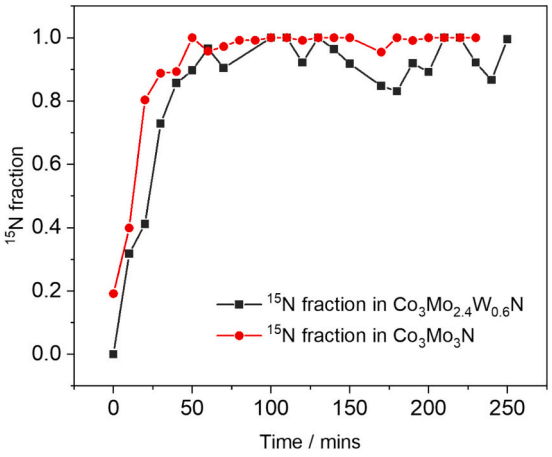

Fig. 8. (Step 5) ^{15}N fractions in the main Fd-3mz phase versus time for sample Co_3Mo_3N and $Co_3Mo_{2.4}W_{0.6}N$ at 650 °C under 3:1 $H_2/^{15}N_2$.

after flowing $^{15}N_2$ for 240 mins, and Tables S12 and S13 contain atom tables for these patterns.

For the Rietveld refinement in GSAS-II, the element entry "N" corresponds to ^{14}N, and the software does not provide a separate scattering length entry for ^{15}N. To model the isotopic composition, element "C" was introduced on the nitrogen site. Carbon was selected because its coherent scattering length (6.65 fm) closely matches that of ^{15}N (6.44 fm), allowing it to be used as a replacement for ^{15}N in the refinement. The ^{15}N and ^{14}N nitrogen site occupancy in the main $Co_3Mo_{2.6}W_{0.4}N$ and Co_3Mo_3N phases and the impurity phase Co_2Mo_3N and $Co_2Mo_{2.6}W_{0.4}N$ were fixed at 1.0 throughout the refinement. The variable was the relative fraction of ^{14}N and ^{15}N. Thus, ^{15}N fraction in Fig. 8 corresponds to the refined $^{15}N / (^{14}N + ^{15}N)$ ratio. To avoid unnecessary correlations, the U_{iso} values of the two species were constrained to be equal, ensuring that the refinement captured only changes in isotopic composition and not differences in thermal parameters. The impurity phases Co_2Mo_3N and $Co_2Mo_{2.6}W_{0.4}N$ exhibited already high ^{15}N weight fractions at the first 10-min time after flowing $^{15}N_2$. Therefore, for all 10-min scans, the ^{15}N fractions of these two impurity phases were fixed at 1.0 and ^{14}N fractions were 0. The weight fractions and U_{iso} of the ^{15}N in the main phases Co_3Mo_3N and $Co_3Mo_{2.6}W_{0.4}N$ were refined, while all other parameters were fixed to the values obtained from the 1-h scans shown in Figs. S7 and S8.

In the case of Co_3Mo_3N, 80% of the ^{14}N was replaced with ^{15}N after approximately 20 min under these conditions and the sites were fully occupied by ^{15}N after about 50 min. For $Co_3Mo_{2.6}W_{0.4}N$, nitrogen exchange proceeded similar but slightly slower; more than 80% ^{15}N occupied the N sites after 50 min with some fluctuations in the values. The results confirm the loss and replacement of the lattice nitrogen within Co_3Mo_3N and $Co_3Mo_{2.6}W_{0.4}N$, with relevance to the possibility of the occurrence of a Mars-van Krevelen mechanism for ammonia synthesis. They also show that the easier loss of nitrogen from $Co_3Mo_{2.6}W_{0.4}N$ is accompanied by fast replacement, since both compounds are fully occupied by ^{15}N at the end of these experiments. These results are a proof of concept which show that the lattice nitrogen mobility of materials can be followed under *operando* conditions more similar to ammonia synthesis reactions using a combination of isotopic labelled ^{15}N and PND.

4. Conclusion

This work demonstrates that combining isotopically labelled gases ($^{14}N_2/^{15}N_2$) with *operando* powder neutron diffraction provides a powerful method for directly probing the lability of bulk lattice nitrogen in metal nitride catalysts during ammonia synthesis. The *operando* study reveals clear differences in the structural responses of Co_3Mo_3N and W-doped $Co_3Mo_{2.6}W_{0.4}N$. Tungsten substitution accelerates the reduction of the Co-Mo nitride, leading to faster formation of Co_6Mo_6N, despite the W-doped material exhibiting lower ammonia synthesis activity. This decoupling between nitrogen lability and catalytic performance highlights that lattice-nitrogen mobility is not the sole descriptor of reactivity in these systems. Both materials show rapid and fully reversible renitridation, confirming their capacity to exchange nitrogen with the gas phase. Isotopic experiments further confirm that lattice nitrogen in both compositions is highly mobile, with complete ^{14}N to ^{15}N exchange occurring within 50–100 min. Overall, this study provides new mechanistic insight into nitrogen lability, phase stability, and isotopic exchange in Co-Mo-(W) nitrides, and establishes *operando* PND as a robust method for probing nitrogen dynamics in a catalytic environment.

CRediT authorship contribution statement

Li Shao: Writing – original draft, Investigation, Data curation. **Angela Daisley:** Writing – original draft, Investigation, Data curation. **Marianna Casavola:** Investigation, Data curation. **Andrew L. Hector:** Writing – review & editing, Writing – original draft, Supervision, Funding acquisition, Conceptualization. **Justin S.J. Hargreaves:** Writing – review & editing, Writing – original draft, Supervision, Funding acquisition, Conceptualization.

Declaration of competing interest

The authors declare no conflict of interest.

Acknowledgements

The authors thank EPSRC for support of this work under grants EP/T028416/1 and EP/T027851/1. STFC are also thanked for provision of time at the ISIS neutron and muon facility under RB2410363, and Dr. Ron Smith and the furnaces team for supporting the experiment. JSJH wishes to take this opportunity acknowledge Harold Kung's many acts of generosity and kindness to him in the past and also to take this opportunity to wish Harold a very happy retirement.

Appendix A. Supplementary data

Supplementary data to this article can be found online at https://doi.org/10.1016/j.cej.2026.173932.

Data availability

The original PND data used in this study are freely available from the ISIS Neutron and Muon Source Data Journal via https://doi.org/10.5286/ISIS.E.RB2410363.

References

[1] Ammonia: Zero-Carbon Fertiliser, Fuel and Energy Store, in: Policy Briefing, The Royal Society, 2020 royalsociety.org/green-ammonia.
[2] P.H. Pfromm, Towards sustainable agriculture: fossil-free ammonia, J. Renewable Sustainable Energy. 9 (2017) 034702, https://doi.org/10.1063/1.4985090.
[3] A. Daisley, J.S.J. Hargreaves, Metal nitrides, the Mars-van Krevelen mechanism and heterogeneously catalysed ammonia synthesis, Catal. Today 423 (2023) 113874, https://doi.org/10.1016/j.cattod.2022.08.016.
[4] K. Zhang, A. Cao, L.H. Wandall, J. Vernieres, J. Kibsgaard, J.K. Nørskov, I. Chorkendorff, Spin-mediated promotion of co catalysts for ammonia synthesis, Science 383 (2024) 1357–1363, https://doi.org/10.1126/science.adn0558.
[5] T.N. Ye, S.W. Park, Y. Lu, J. Li, M. Sasase, M. Kitano, T. Tada, H. Hosono, Vacancy-enabled N_2 activation for ammonia synthesis on an Ni-loaded catalyst, Nature 583 (2020) 391–395, https://doi.org/10.1038/s41586-020-2464-9.
[6] T.N. Ye, S.W. Park, Y. Lu, J. Li, M. Sasase, M. Kitano, H. Hosono, Contribution of nitrogen vacancies to ammonia synthesis over metal nitride catalysts, J. Am. Chem. Soc. 142 (2020) 14374–14383, https://doi.org/10.1021/jacs.0c06624.
[7] S.M. Hunter, D. Mckay, R.I. Smith, J.S.J. Hargreaves, D.H. Gregory, Topotactic nitrogen transfer: structural transformation in cobalt molybdenum nitrides, Chem. Mater. 22 (2010) 2898–2907, https://doi.org/10.1021/cm100208a.

[8] C.D. Zeinalipour-Yazdi, J.S.J. Hargreaves, C.R.A. Catlow, Nitrogen activation in a Mars–van Krevelen mechanism for ammonia synthesis on Co_3Mo_3N, J. Phys. Chem. C 119 (2015) 28368–28376, https://doi.org/10.1021/acs.jpcc.5b06811.
[9] C.D. Zeinalipour-Yazdi, J.S.J. Hargreaves, C.R.A. Catlow, Low-T mechanisms of ammonia synthesis on Co_3Mo_3N, J. Phys. Chem. C 122 (2018) 6078–6082, https://doi.org/10.1021/acs.jpcc.7b12364.
[10] S.M. Hunter, D.H. Gregory, J.S.J. Hargreaves, M. Richard, D. Duprez, N. Bion, A study of $^{15}N/^{14}N$ isotopic exchange over cobalt molybdenum nitrides, ACS Catal. 3 (2013) 1719–1725, https://doi.org/10.1021/cs400336z.
[11] C.J.H. Jacobsen, Novel class of ammonia synthesis catalysts, Chem. Commun. 12 (2000) 1057–1058, https://doi.org/10.1039/B002930K.
[12] R. Kojima, K.-I. Aika, Cobalt molybdenum bimetallic nitride catalysts for ammonia synthesis: part 1. Preparation and characterization, Appl. Catal. A Gen. 215 (2001) 149–160, https://doi.org/10.1016/S0926-860X(01)00529-4.
[13] R. Kojima, K.-I. Aika, Cobalt molybdenum bimetallic nitride catalysts for ammonia synthesis: part 2. Kinetic study, Appl. Catal. A Gen. 218 (2001) 121–128, https://doi.org/10.1016/S0926-860X(01)00626-3.
[14] R. Kojima, K.-I. Aika, Cobalt molybdenum bimetallic nitride catalysts for ammonia synthesis: part 3. Reactant gas treatment, Appl. Catal. A Gen. 219 (2001) 157–170, https://doi.org/10.1016/S0926-860X(01)00678-0.
[15] P. Adamski, D. Moszynski, M. Nadziejko, A. Komorowska, A. Sarnecki, A. Albrecht, Thermal stability of catalyst for ammonia synthesis based on cobalt molybdenum nitrides, Chem. Pap. 73 (2019) 851–859, https://doi.org/10.1007/s11696-018-0642-0.
[16] A. Daisley, L. Costley-Wood, J.S.J. Hargreaves, The role of composition and phase upon the lattice nitrogen reactivity of ternary molybdenum nitrides, Top. Catal. 64 (2021) 1021–1029, https://doi.org/10.1007/s11244-021-01432-1.
[17] S. Al Sobhi, I. Alshibane, C.R.A. Catlow, A. Daisley, J.S.J. Hargreaves, A.L. Hector, M.D. Higham, C.D. Zeinalipour-Yazdi, A comparison of the reactivity of the lattice nitrogen in tungsten substituted Co_3Mo_3N and Ni_2Mo_3N, ChemSusChem 16 (2023) e202300945, https://doi.org/10.1002/cssc.202300945.
[18] J.O. Conway, T.J. Prior, Interstitial nitrides revisited – a simple synthesis of M_xMo_3N (M = Fe, Co, Ni), J. Alloys Compd. 774 (2019) 69–74, https://doi.org/10.1016/j.jallcom.2018.09.307.
[19] B.H. Toby, R.B. Von Dreele, GSAS-II: the genesis of a modern open-source all purpose crystallography software package, J. Appl. Crystallogr. 46 (2013) 544–549, https://doi.org/10.1107/S0021889813003531.
[20] D. Moszynski, Controlled phase composition of mixed cobalt molybdenum nitrides, Int. J. Refract. Met. Hard Mater. 41 (2013) 449–452, https://doi.org/10.1016/j.ijrmhm.2013.06.002.
[21] P. Adamski, D. Moszynski, A. Komorowska, M. Nadziejko, A. Sarnecki, A. Albrecht, Ammonolysis of cobalt molybdenum oxides - in situ XRD study, Inorg. Chem. 57 (2018) 9844–9850, https://doi.org/10.1021/acs.inorgchem.8b00685.
[22] D. Mckay, D.H. Gregory, J.S.J. Hargreaves, S.M. Hunter, X. Sun, Towards nitrogen transfer catalysis: reactive lattice nitrogen in cobalt molybdenum nitride, Chem. Commun. 29 (2007) 3051–3053, https://doi.org/10.1039/B707913C.
[23] S.M. Hunter, Molybdenum nitrides: structural and reactivity studies, in: PhD Thesis, University of Glasgow, 2012. https://theses.gla.ac.uk/id/eprint/3221.
[24] M.D. Higham, C.D. Zeinalipour-Yazdi, J.S.J. Hargreaves, C.R.A. Catlow, Mechanism of ammonia synthesis on Fe_3Mo_3N, Faraday Discuss. 243 (2023) 77–96, https://doi.org/10.1039/D2FD00148A.